A One-step, Template-free Synthesis, Characterization, Optical and Magnetic Properties of $Zn_{1-x}Mn_xTe$ Nanosheets

Sayan Bhattacharyya,[†] D. Zitoun,[‡] Y. Estrin,[§] O. Moshe,[§] D. H. Rich,[§] and A. Gedanken*,[†]

Department of Chemistry and Kanbar Laboratory for Nanomaterials at the Bar-Ilan University Center for Advanced Materials and Nanotechnology, Bar-Ilan University, Ramat-Gan 52900, Israel, ICGM-AIME, Université Montpellier II, CC15, Place Bataillon 34095 Montpellier, France, and Department of Physics, The Ilse Katz Institute for Nanoscience and Nanotechnology, Ben-Gurion University of the Negev, P.O.B 653, Beer-Sheva 84105, Israel

Received October 12, 2008. Revised Manuscript Received November 26, 2008

The $Zn_{1-x}Mn_xTe$ nanosheets were synthesized by the one-pot RAPET (reaction under autogenic pressure at elevated temperature) approach. The efficient replacement of Zn by Mn within the $Zn_{1-x}Mn_xTe$ lattice was confirmed from electron paramagnetic resonance (EPR) experiments. The (111) facets form the main surfaces of the ~38 nm thick nanosheet structures. Mn catalyzes the formation of a small amount of nanorods (diameter ~2.6 nm) alongside the nanosheet structures. The magnetic measurements (EPR and SQUID) confirm the +II state of manganese in all the products. Two local environments with strong parallel or antiparallel coupling of the Mn spins exist, specially in the case of Mn:Zn = 0.01 (T1). T1 exhibits a relatively large magnetic moment of 0.12 μ_B at $\mu_0 H = 1.0$ T and reflects the contribution of a paramagnetic phase (with antiferromagnetic interactions) and of a ferromagnetic phase. Variable temperature cathodoluminescence measurements were performed for all samples and showed distinct ZnTe near-band edge and Mn-related luminescence. An intense and broad intra-Mn^{2+} transition at relatively large Mn alloy compositions of 10−15% is further consistent with an efficient incorporation of Mn within the host ZnTe lattice. The template-free formation of the nanosheets and nanorods are explained with the help of controlled experiments. From the technological point of view, the organization of the spintronic nanomaterials into 2D or 3D architectures is important for their assemblage onto a microscopic chip and the $Zn_{1-x}Mn_xTe$ nanosheets is a major breakthrough toward realization of such functionality.

1. Introduction

Recently, there has been growing interest in the Mn-based II−VI compound diluted magnetic semiconductor (DMS) nanostructures.[1] This interest is stimulated by the possible realization of high performance optoelectronic devices due to the wide direct band gap and magnetic, magneto-electronic and magneto-optical properties for spintronics applications.[2] Mn^{2+} acts as a paramagnetic center ($S = 5/2$) and sp−d exchange interaction occurs between the electron/hole band states of the semiconductors and the Mn^{2+} $3d^5$ electron states in the DMS nanocrystals.[2b] However, the fact that Mn is actually embedded inside the semiconductor unit cell is important for obtaining high-quality Mn-doped II−VI DMS nanomaterials.[1a] Although Mn^{2+} ions can be incorporated thermodynamically up to their solid solubility limit (~50%), Mn has a tendency to be expelled from the semiconductor nanocrystal surface.[1a,3] Zinc telluride (ZnTe) is an intrinsic wide-gap semiconductor material with a band gap of 2.23−2.25 eV, having a cubic crystal structure with a wide range of practical applications.[4] Because of the possibility of hole-induced ferromagnetism and magneto-electronics applications, $Zn_{1-x}Mn_xTe$ single crystals, thin films, and quantum dots were extensively researched over the years.[2,5,6] However, future applications related to high-density magnetic recording and waveguide-type optical communications require a fine control of the materials at the nanoscale level, and organization of the spintronic materials into two-

* Corresponding author. E-mail: gedanken@mail.biu.ac.il.
[†] Bar-Ilan University.
[‡] Université Montpellier II.
[§] Ben-Gurion University of the Negev.

(1) (a) Erwin, S. C.; Zu, L.; Haftel, M. I.; Efros, A. L.; Kennedy, T. A.; Norris, D. J. *Nature* **2005**, *436*, 91–94. (b) Kwak, W. C.; Sung, Y. M.; Kim, T. G.; Chae, W. S. *Appl. Phys. Lett.* **2007**, *90*, 173111. (c) Pradhan, N.; Peng, X. G. *J. Am. Chem. Soc.* **2007**, *129*, 3339–3347. (d) Bhattacharyya, S.; Perelshtein, I.; Moshe, O.; Rich, D. H.; Gedanken, A. *Adv. Funct. Mater.* **2008**, *18*, 1641–1653.

(2) (a) Dietl, T.; Onno, H.; Matsukura, F.; Cibert, J.; Ferrand, D. *Science* **2000**, *287*, 1019–1022. (b) Zutic, I.; Fabian, J; Das Sarma, S. *Rev. Mod. Phys* **2004**, *76*, 323–410.

(3) Norris, D. J.; Yao, N.; Charnock, F. T.; Kennedy, T. A. *Nano Lett.* **2001**, *1*, 3–7.

(4) Kotlyarchuk, B.; Savchuk, V. *Phys. Status Solidi B* **2007**, *244*, 1714–1719.

(5) (a) Ferrand, D.; Cibert, J.; Bourgognon, C.; Tatarenko, S.; Wasiela, A.; Fishman, G.; Bonanni, A.; Sitter, H.; Koleśnik, S.; Jaroszyński, J.; Barcz, A.; Dietl, T. *J. Cryst. Growth* **2000**, *214/215*, 387–390. (b) Kępa, H.; Khoi, L. V.; Brown, C. M.; Sawicki, M; Furdyna, J. K.; Giebultowicz, T. M.; Dietl, T. *Phys. Rev. Lett.* **2003**, *91*, 087205. (c) Ferrand, D.; Wasiela, A.; Tatarenko, S.; Cibert, J.; Richter, G.; Grabs, P.; Schmidt, G.; Molenkamp, L. W.; Dietl, T. *Solid State Commun.* **2001**, *119*, 237–244.

(6) (a) Maingault, L.; Besombes, L.; Léger, Y.; Bougerol, C.; Mariette, H. *Appl. Phys. Lett.* **2006**, *89*, 193109. (b) Khoi, L. V.; Avdonin, A; Gałązka, R. R.; Lentze, M.; Kehl, C; Geurts, J.; Eyring, M.; Astakhov, G.; Ossau, W. *Phys. Status Solidi B* **2007**, *244*, 1680–1684. (c) Liu, X.; Bindley, U.; Sasaki, Y.; Furdyna, J. K. *J. Appl. Phys.* **2002**, *91*, 2859–2865. (d) Shand, P. M.; Christianson, A. D.; Pekarek, T. M.; Martinson, L. S.; Schweitzer, J. W.; Miotkowski, I.; Crooker, B. C. *Phys. Rev. B* **1998**, *58*, 12876–12882. (e) Masterson, H. J.; Lunney, J. G.; Coey, J. M. D. *J. Appl. Phys.* **1997**, *81*, 799–805.

10.1021/cm8027737 CCC: $40.75
Published on Web 12/30/2008

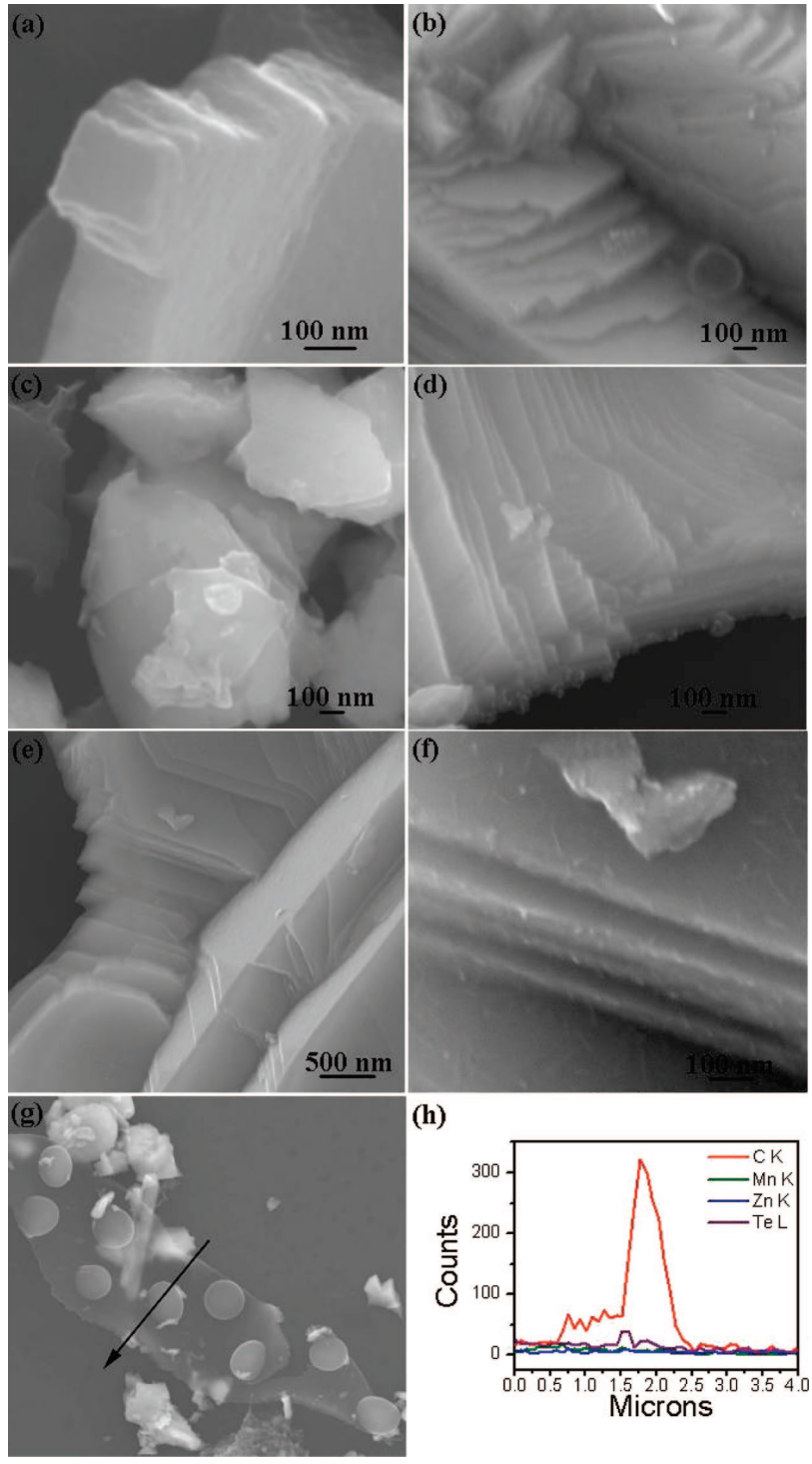

Figure 1. HRSEM images of (a) T0, (b) T1, (c) T2, (d) T3, (e) T4, (f) magnified view in T4 showing the thickness of the nanosheets, (g) carbon submicron spheres located on the top of a carbon nanosheet, and (h) elemental line scan of the carbon nanosheet in g. The nanosheet region is dominated by the C-signal.

dimensional (2D) or three-dimensional (3D) architectures on a microscopic chip.[7,8] Moreover, the self-assembly of nanoscale structures is an attractive nanofabrication bottom-up approach, as compared to lithography techniques, for the fabrication of ever smaller devices in microelectronics and for the magnetic-storage industry.

Thus, because of the technological importance of the 2D nanostructures, a wide range of nanosheets such as MgO,

(7) Osada, M.; Ebina, Y.; Takada, K.; Sasaki, T. *Adv. Mater.* **2006**, *18*, 295–299.

(8) (a) Tombros, N.; Jozsa, C.; Popinciuc, M.; Jonkman, H. T.; van Wees, B. J. *Nature* **2007**, *448*, 571–574. (b) Deng, W. Q.; Matsuda, Y.; Goddard III, W. A. *J. Am. Chem. Soc.* **2007**, *129*, 9834–9835. (c) Dumestre, F.; Chaudret, B.; Amiens, C.; Renaud, P.; Fejes, P. *Science* **2004**, *303*, 821–823.

(9) (a) Zhu, K.; Hu, J.; Kübel, C.; Richards, R. *Angew. Chem., Int. Ed.* **2006**, *45*, 7277–7281. (b) Xu, Y.; Chen, D.; Jiao, X.; Ba, L. *J. Phys. Chem. C* **2007**, *111*, 6–9. (c) Zhao, J.; Ye, C.; Fang, X.; Yan, P.; Zhang, L. *Mater. Chem. Phys.* **2006**, *99*, 206–209. (d) Yang, X.; Makita, Y.; Liu, Z.; Sakane, K.; Ooi, K. *Chem. Mater.* **2004**, *16*, 5581–5588. (e) Fukuda, K.; Ebina, Y.; Shibata, T.; Aizawa, T.; Nakai, I.; Sasaki, T. *J. Am. Chem. Soc.* **2007**, *129*, 202–209.

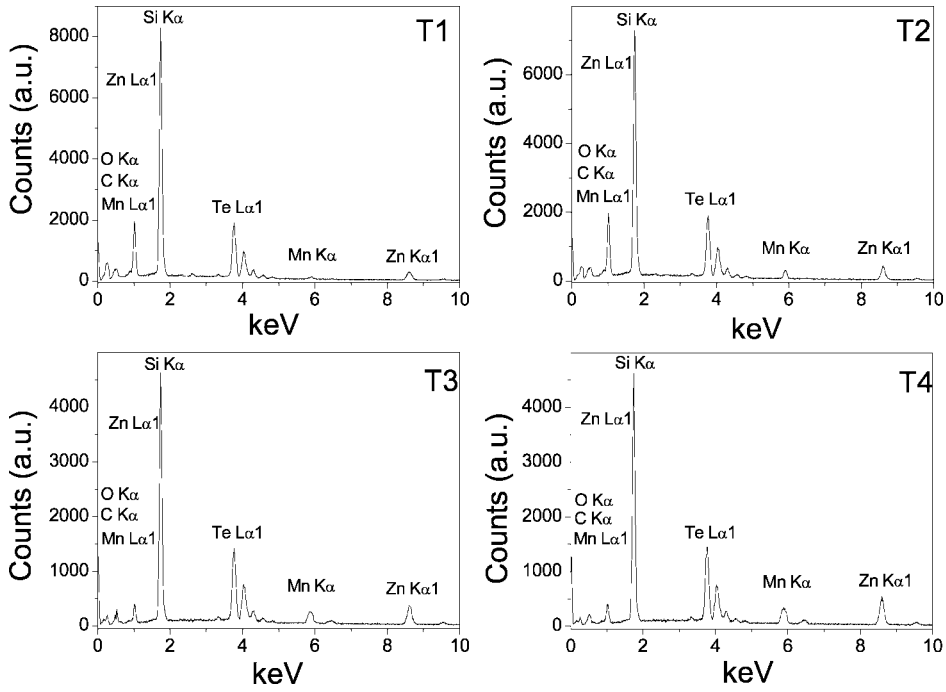

Figure 2. EDS results coupled with HRSEM.

TiO_2, CuI, CdS, MnO_2,[9] and nanoplates such as ZnS, In_2S_3, Ag, LnO_2, and ZnO[10] have been discussed in the literature. Apart from these, telluride nanosheets such as Cu_2Te, Ag_2Te, and Bi_2Te_3 were fabricated using hydrothermal synthesis.[11] To the best of our knowledge, reports on DMS nanosheets/nanoplates are scarce and we could find only one previous report on Co-doped TiO_2 nanosheets with quartz glass and Si wafer as substrates.[7] Moreover, ZnTe is not a well developed system like CdSe, CdTe, or ZnSe, and several difficulties arise in ZnTe system for the controlled growth in high-temperature colloidal reactions. In the current study, we report on the successful template-free, one-step, bottom-up synthesis of Mn-doped ZnTe nanosheets via the straightforward RAPET (reactions under autogenic pressure at elevated temperature) approach. The RAPET technique is cheaper and much simpler than the other methods and avoids the use of solvents.

2. Results and Discussion

The inductively coupled plasma (ICP) experiments confirmed the composition of the solid products according to the Mn:Zn atomic ratio of 0, 0.01, 0.043, 0.092, and 0.187 and are designated as T0, T1, T2, T3, and T4, respectively, in subsequent discussions in the paper. Figure 1a−f shows the high-resolution scanning electron microscope (HRSEM) images of the polycrystalline nanosheets.

As is evident from the images, all the nanosheets are highly organized and self-assembled, resembling the steps of a staircase. In T0, the average length (L) and breadth (B) of the nanosheets are 173−276 and 700 nm, respectively. In T1, the breadth of the nanosheets is 820 nm with a thickness of 22 ± 4 nm. In T2, the dimensions are B = 450−650 nm and L = 820 nm to 1.1 μm. The nanosheets of T3 are 2.6 μm in length. The T4 nanosheets (L = 1.6 μm; B = 1.2 μm) are formed consisting of a single crystal (Figure 1e). In Figure 1f, we present a magnified view of the edge of the nanosheets in T4 and the average thickness of the sheets is estimated to be 38 ± 7 nm. A few nanorods (D = 3 ± 1 nm; L = 100 ± 4 nm) are observed on the surface of the nanosheet. Apart from the $Zn_{1-x}Mn_xTe$ nanosheets, carbon nanosheets (L = 11 μm; B = 2.6 μm) and submicrometer carbon spheres are also formed within the Swagelok reactor during decomposition of the starting acetate precursors (Figure 1g). The amount of carbon determined from C, H, N analysis is 2.5, 1.2, 1.0, 0.9, and 1.0% in T0, T1, T2, T3, and T4 products, respectively.

The results obtained from energy-dispersive X-ray spectroscopy (EDS) coupled with HRSEM are shown in Figure 2. The dispersion of the sample in dry ethanol was spread onto a silicon wafer and dried in a glovebox. The EDS spectra were recorded at six different locations to ascertain the homogeneity of the Mn incorporation in the nanosheets. The Mn:Zn atomic ratios obtained from the EDS results are 0.01(0), 0.04(0), 0.09(0), and 0.18(0) for T1, T2, T3, and T4, respectively. These values match well with the quantitative analysis by ICP measurements. The precise content of the nanosheets in T4 was confirmed by employing a highly sensitive, wave-dispersive X-ray analyzer (WDX), which is coupled to the HRSEM instrument. The selected area for the elemental X-ray dot mapping is shown in Figure 3a. The contents of C, Zn, Te, and Mn are presented in Figures 3 c−f, respectively. The Si signal outside the sample region

(10) (a) Zhou, G. T.; Wang, X.; Yu, J. C. *Cryst. Growth Des.* **2005**, *5*, 1761–1765. (b) Park, K. H.; Jang, K.; Son, S. U. *Angew. Chem., Int. Ed.* **2006**, *45*, 4608–4612. (c) Xiong, Y.; Washio, I.; Chen, J.; Sadilek, M.; Xia, Y. *Angew. Chem., Int. Ed.* **2007**, *46*, 4917–4921. (d) Si, R.; Zhang, Y. W.; You, L. P.; Yan, C. H. *Angew. Chem., Int. Ed.* **2005**, *44*, 3256–3260. (e) Zhan, J.; Bando, Y.; Hu, J.; Golberg, D.; Kurashima, K. *Small* **2006**, *2*, 62–65.

(11) (a) Zhang, L.; Zhihui, A.; Jia, F.; Liu, L.; Hu, X.; Yu, J. C. *Chem. Eur. J.* **2006**, *12*, 4185–4190. (b) Zhao, X. B.; Ji, X. H.; Zhang, Y. H.; Cao, G. S.; Tu, J. P. *Appl. Phys. A: Mater. Sci. Process.* **2005**, *80*, 1567–1571. (c) Zhang, Y. H.; Zhu, T. J.; Tu, J. P.; Zhao, X. B. *Mater. Chem. Phys.* **2007**, *103*, 484–488.

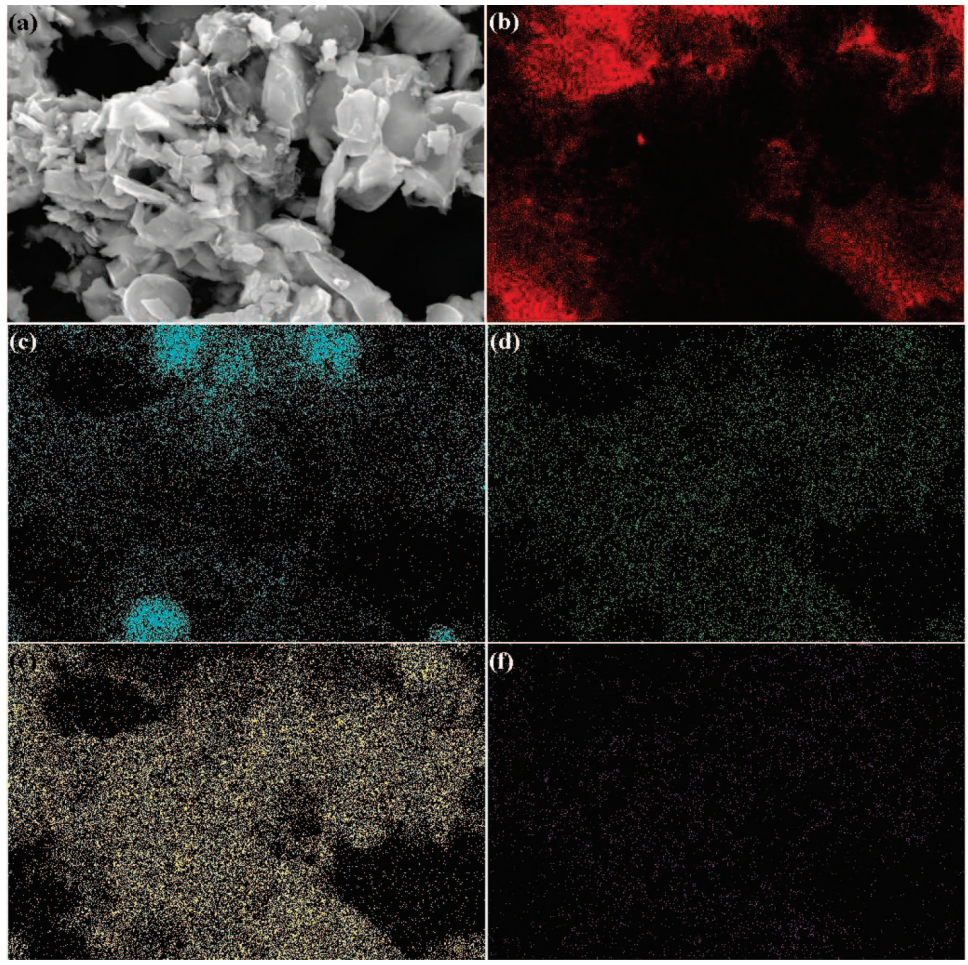

Figure 3. (a) Selected image of T4 for X-ray dot mapping. X-ray dot mapping for (b) Si, (c) C, (d) Zn, (e) Te, and (f) Mn.

in Figure 3b appears from the Si wafer substrate. A few C spheres and a thin layer of carbon over the nanosheets are observed in Figure 3c. The Zn, Te, and Mn signals are detected within the position of the nanosheets. The uniform distribution of Mn over the nanosheets in Figure 3f confirms uniform manganese doping.

The TEM images in Figure 4 mirror the nanostructures observed in HRSEM. The average breadth of the nanosheets increases from 100 to 370 nm for T0 to T2. In Figure 4d, two nanosheets ($B = 130$ nm) lie one on top of one another. A few nanorods dangling freely from the nanosheet surface are shown with arrows.

The dark lines observed on the surface of the nanosheet of T4 (Figure 4e) are the possible defects and cracks on the nanosheet structure. The selected area diffraction (SAED) pattern of the nanosheet in Figure 4e was indexed to the ZnTe lattice and indicates the high crystallinity of the nanosheets. The high-resolution image of T4 (Figure 4g) shows the interlayer spacing of 0.352 nm and matches well with the JCPDS card no. 89−3054 for the (111) plane of ZnTe. Figure 4h presents a close view of a single nanorod of aspect ratio = 13.5 (length = 35 nm and diameter = 2.6 nm), whereas the inset picture shows the lattice fringes matching with the (111) plane of ZnTe. However, the preferred growth direction of the nanorods is not ascertained since the lattice fringes are not perpendicular to the nanorod axis. Interestingly, a larger amount of nanorods is detected for samples with an increase in the Mn concentration, which makes it obvious that the nanorods are formed due to the catalytic action of Manganese.[12] The composition of the nanorods were determined based on EDS analysis of 3 nanorods each in T3 and T4. The nanorods are composed of 55(2)% Te and the Mn:Zn atomic ratios are 0.094(3) and 0.19(1) for T3 and T4, respectively. The TEM image of the carbon nanosheet in Figure 4i represents an amorphous or semicrystalline nature.

The X-ray diffraction (XRD) patterns in Figure 5 for all the products show the face-centered cubic ZnTe phase and match well the JCPDS card No. 89−3054. Interestingly, the relative intensity of the XRD peaks varied with the increase in Mn concentration and with respect to pristine ZnTe (T0). In T0, the peak with 100% relative intensity is indexed to the (220) reflection, while for the Mn-doped products, the (111) plane corresponds to the most intense peak. The peak intensity ratio of the planes varied with the orientation of the nanosheets on the substrate in the XRD experiment.[9b,13] This is observed for T4, where the (111) planes tend to be preferentially oriented parallel to the surface of the substrate. This is in accordance with the interlayer lattice spacing in Figure 4g.

(12) Martelli, F.; Piccin, M.; Bais, G.; Jabeen, F.; Ambrosini, S.; Rubini, S.; Franciosi, A. *Nanotechnology* **2007**, *18*, 125603.
(13) Oaki, Y.; Imai, H. *Angew. Chem., Int. Ed.* **2007**, *46*, 4951–4955.

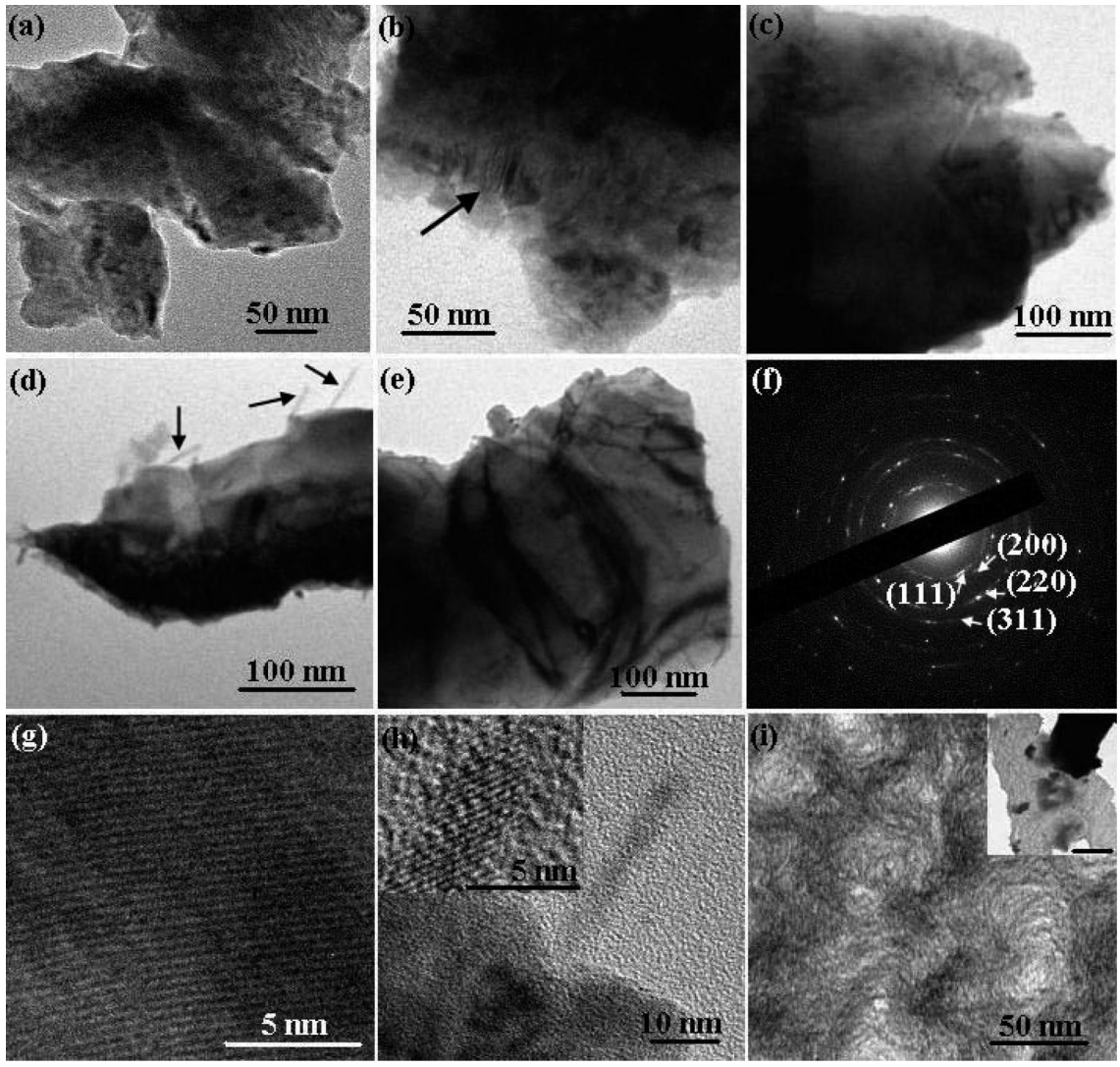

Figure 4. TEM images of (a) T0, (b) T1 (arrow shows the parallel alignment of layers seen from side), (c) T2, (d) T3, (e) T4, (f) SAED pattern of the region shown in e, (g) HRTEM image of a nanosheet in T4, (h) magnified TEM view of the edge of a nanosheet (inset shows HRTEM image of the nanorod protruding out from the nanosheet surface), (i) magnified TEM image of a carbon nanosheet (inset shows the whole carbon nanosheet); scale bar = 1 μm.

During the template-free formation of the nanosheets, the Zn- and Mn-acetates initially decompose into their gaseous state, along with gaseous Te, when heated to 900 °C inside the Swagelok reactor. The decomposition of acetates involves the following steps: (i) $M(CH_3COO)_2 \cdot xH_2O \rightarrow M(CH_3COO)_2 + xH_2O$; (M = Zn, Mn); (ii) $M(CH_3COO)_2 \rightarrow MCO_3 + CH_3COCH_3$; (iii) $CH_3COCH_3 \rightarrow CO + C_2H_6$; (iv) $2CO \rightarrow C + CO_2$ (Boudouard reaction); (v) $MCO_3 \rightarrow MO + CO_2$.[14] Gaseous Te reacts with $(Zn_{1-x}Mn_x)$-O to form $Zn_{1-x}Mn_xTe$ via the following reaction: $2\ Zn_{1-x}Mn_xO + 2\ Te \rightarrow 2\ Zn_{1-x}Mn_xTe + O_2$. In a closed Swagelok reaction, the products of the dissociation reaction remain in the gas phase and solidify right after their formation. A little stoichiometric excess of Te was required at 900 °C to avoid any $Zn_{1-x}Mn_xO$ impurity phase formation. We performed a few blank experiments to determine the possible factor behind the 2D nanosheet growth. The RAPET reaction between Zn- and Mn-acetates (in the absence of Te) at 600−1000 °C yielded 50−100 nm platelet-shaped nanoparticles (see the Supporting Information). Mn-acetate and Te react to form a mixture of nanosheets ($L \approx 400$ nm) with spherical ~10 nm particles attached to the nanosheets and rod structures of length = 450−600 nm and breadth = 90 ± 5 nm. The reaction between Zn-acetate, Mn-acetate and Te at lower temperatures (≤800 °C) could form incomplete nanosheets, with gaps within the sheet structure. Even at temperatures below 900 °C, $Zn_{1-x}Mn_xO$ was present in addition to $Zn_{1-x}Mn_xTe$. Hence, it is clear that the proper decomposition of Te powder into gaseous Te is the essential criterion for forming nanosheets, which is achieved at 900 °C. ZnTe crystallizes in the cubic sphalerite structure, where Zn and Te are tetrahedrally coordinated with ABCABC packing along the *c*-axis. This can be viewed as a layered structure, where atomic layers arrange in the order of $Te^{(1)}-Zn-Te^{(2)}-Zn-Te^{(1)}$ along the *c*-axis direction. The superscripts denote the two different planes of Te atoms. A covalent bond exists between neighboring Zn and Te atoms, whereas two Te layers are bonded through van der Waals interactions. In the case of Zn or Te terminated crystal surfaces, the Zn or Te atoms from the gaseous phase cannot

(14) Pol, S. V.; Pol, V. G.; Felner, I.; Gedanken, A. *Eur. J. Inorg. Chem.* **2007**, *208*, 9–2096.

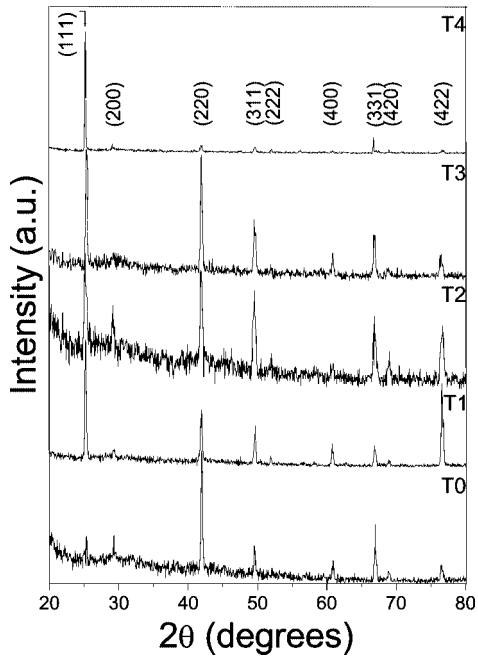

Figure 5. XRD pattern taken from the synthesized products.

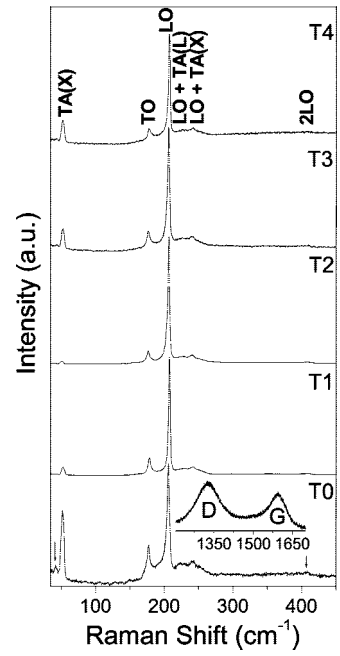

Figure 6. Raman spectra of the products.

attach themselves to the respective sides since the van der Waals bonding is sufficiently weak to hold the atom on the surface. Hence, crystal growth in the *a*- and *b*-axis becomes more favored than in the *c*-direction, which ultimately results in the 2D growth of the nanosheets.[11b] The individual nanosheets might be joined through the electrostatic interaction between the oppositely charged species. The perfect attachment of the crystal faces gives rise to the ordered cubic or rectangular shaped nanosheets (Figure 1). The formation of a small concentration of the nanorods occurs independently because of the catalytic action of Mn. The nanosheets are preferentially formed in larger quantities because the ultrahigh-density and highly ordered packing superstructure of the nanosheets is a thermodynamically favorable process due to the decreased surface energy.[10e,15]

Figure 6 shows the room-temperature vibrational Raman spectra of the products. Raman spectroscopy is a sensitive method to ascertain the crystal quality because the extended defects can give rise to broadening of the Raman peaks.[16] The Raman peaks for $Zn_{1-x}Mn_xTe$ are observed at 42, 52, 177, 206, 223, 242, and 410 cm^{-1}. The intensity of the Raman peaks are most pronounced in the pristine ZnTe (T0). The Raman peaks at 177 and 206 cm^{-1} are attributed to the transverse optic (TO) and longitudinal optic (LO) phonon modes of ZnTe, respectively.[17] The low-frequency disorder induced feature is identified as the one-phonon density of states TA(X) at 52 cm^{-1}. The higher frequency features at 223 and 242 cm^{-1} are attributed to the combination of LO phonon with transverse acoustic phonon at L and X points of the Brillouin zone, LO + TA(L) and LO + TA(X), respectively. The 2LO phonon mode of ZnTe is observed at 410 cm^{-1}.[16] The peak at 42 cm^{-1} is due to probable surface defects. With increasing Mn concentration from T0 to T4, the splitting between LO and TO phonon modes increases by 1.3 cm^{-1} because of the relative shift of these peaks. The Raman spectrum in the 1200−1700 cm^{-1} region is characteristic of disordered graphitic carbon present in all the products in the form of C-spheres and carbon nanosheets. The Raman peaks at 1330 and 1600 cm^{-1} are the D and G bands, respectively. The D-band is attributed to the Raman-inactive A_{1g} vibration mode assigned to the vibrations of carbon atoms with dangling bonds in planar terminations of disordered graphite.[18] The G-band is the Raman active optical mode E_{2g} of 2D graphite and is closely related to the vibrations in sp^2 bonded carbon atoms.[19] The relatively sharp and symmetric Raman peaks suggest that the $Zn_{1-x}Mn_xTe$ nanosheets are highly crystalline and single phase.

To further examine the optically active nature of the $Zn_{1-x}Mn_xTe$ nanosheets, we performed cathodoluminescence (CL) spectroscopy for temperatures ranging from 60 to 300 K. The electron beam (e-beam) was raster scanned over an area of 256 × 192 μm^2 for each sample to yield an effective spatial average of the CL spectra for this area. Luminescence studies of pure epitaxial $Zn_{1-x}Mn_xTe$ layers are rare.[20] Yu et al. have performed photoluminescence (PL) measurements of $Zn_{1-x}Mn_xTe$ epilayers grown on the GaAs (100) substrates by hot-wall epitaxy and demonstrated that PL associated with the intra-Mn^{2+} transition dominates the total emission for Mn compositions $x > 0.08$.[20a]

Stack plots of CL spectra for various temperatures between 60 and 300 K are shown in Figure 7 for the four samples T1−T4, respectively. The peak height for each CL spectrum

(15) Wu, H. Y.; Huang, W. L.; Huang, M. H. *Cryst. Growth Des.* **2007**, *7*, 831–835.
(16) Kume, Y.; Guo, Q.; Tanaka, T.; Nishio, M.; Ogawa, H.; Shen, W. *J. Cryst. Growth* **2007**, *298*, 441–444.
(17) Peterson, D. L.; Petrou, A.; Giriat, W.; Ramdas, A. K.; Rodriguez, S. *Phys. Rev. B* **1986**, *33*, 1160–1165.
(18) Shimodaira, N.; Masui, A. *J. Appl. Phys.* **2002**, *92*, 902–909.
(19) Barbarossa, V.; Galluzzi, F.; Tomaciello, R.; Zanobi, A. *Chem. Phys. Lett.* **1991**, *185*, 53–55.
(20) (a) Yu, Y.-M.; O, B.; Yoon, M.-Y.; Kim, J. B.; Choi, Y. D. *Thin Solid Films* **2003**, *426*, 265–270. (b) Khoi, L. V.; Kossut, J.; Galazka, R. R. *J. Superconduct. Novel Magn.* **2003**, *16*, 427–429. (c) Yang, T.-R.; Lu, C.-C.; Dvoynenko, M. M.; Chou, W. C. *Phys. B* **2003**, *329−333*, 928–929.

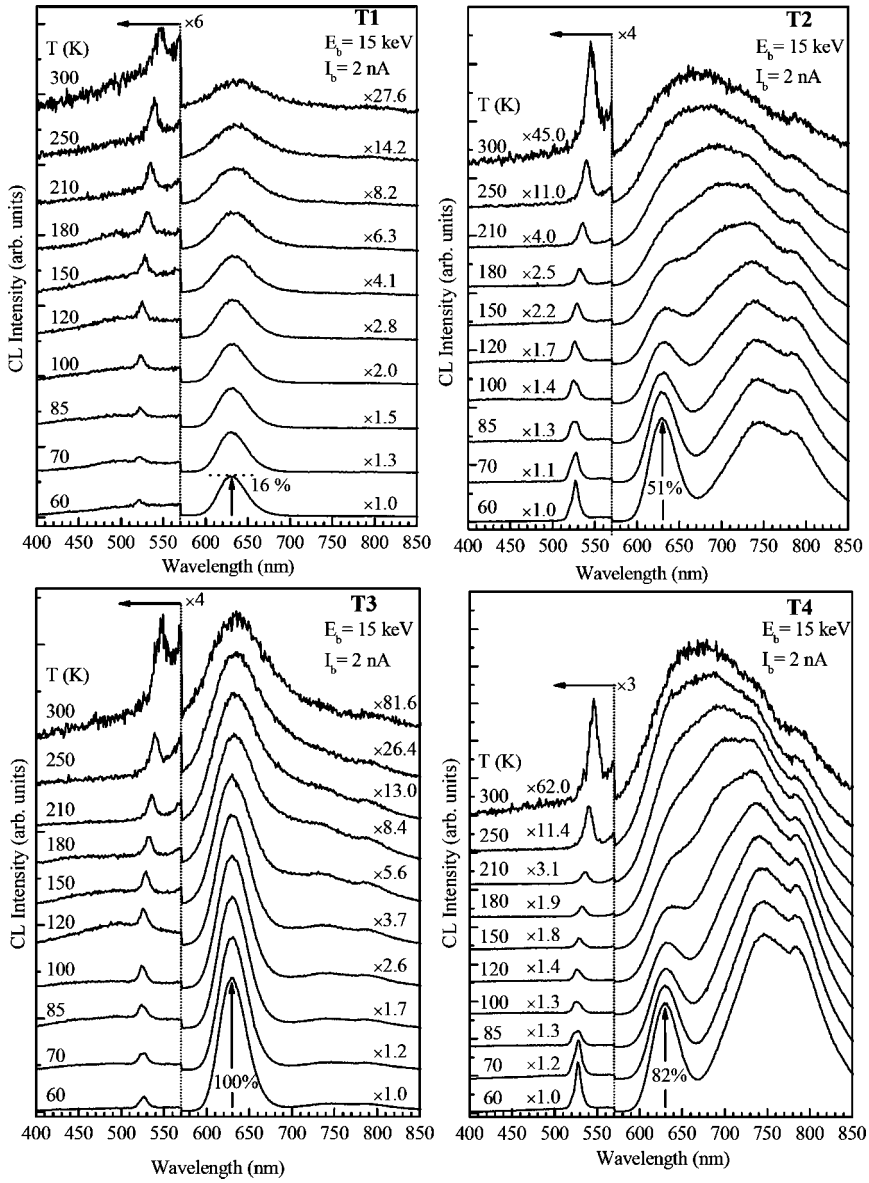

Figure 7. CL spectra of samples T1−T4 for various temperatures in the 60 K ≤ T ≤ 300 K range. The spectra are scaled for each group of samples according to the indicated scale factors. The absolute CL intensities for samples T1, T2, and T4 are compared with the maximum emission of sample T3 whose reference is defined as 100% for the Mn^{2+}-related emission at 60 K.

has been normalized in each panel according to scale factors, as indicated for all spectra in the stack plots. Distinct emission in the wavelength range of 520−540 nm is attributed to the ZnTe near band gap excitonic recombination. Typical red-shifts of ∼20 nm are observed as the temperature is raised from 60 to 300 K, consistent with the expected temperature dependence of the ZnTe bandgap.[20a] The emissions centered at ∼630 nm in Figure 7 are attributed to the $^4T_1$ to $^6A_1$ transition in the Mn^{2+} ion (i.e., the intra Mn^{2+} transition) in $Zn_{1-x}Mn_xTe$ crystalline layers.[21] The broad and intense Mn-related emission is a strong indication that Mn is well incorporated both structurally and electronically into the host ZnTe host crystal. In Figure 7, various structures are observed toward longer wavelengths ($\lambda \gtrsim 650$ nm) relative to the intra Mn^{2+} emission and are particularly intense for the T2 and T4 samples. Such emissions are attributed to presence of defect, impurity and possibly surface recombination. A striking aspect of the data is that the intra Mn^{2+} emission intensity rapidly decreases relative to that of the defect-related emissions as the temperature increases. For $T \gtrsim 150$ K, the intra-Mn^{2+} emission is evidently dominated by defect-related emissions for samples T2 and T4, to the extent in which it is no longer possible to resolve a distinct Mn^{2+}-related peak. The absence of intense defect related features together with the strong and distinct Mn^{2+}-related peak for samples T1 and T3 further attests to a good crystalline quality for these nanosheets.

In addition to the scale factors that indicate the relative intensity for each CL spectrum at varying temperatures, the absolute intensity of emission for each sample is indicated by a comparison of the intensities of the Mn^{2+}-related peak at $T = 60$ K for the four samples, T1−T4. Sample T3

(21) (a) Lee, Y. R.; Ramdas, A. K.; Aggarwal, R. L. *Phys. Rev. B* **1986**, *33*, 7383–7385. (b) Waldmann, H.; Benecke, C.; Busse, W.; Gumlich, H.-E.; Krost, A. *Semicond. Sci. Technol.* **1989**, *4*, 71–76. (c) Crabtree, D. F. *Phys. Status Solidi A* **1974**, *22*, 543–552.

(22) Kanaya, K.; Okayama, S. *J. Phys. D: Appl. Phys.* **1972**, *5*, 43–58.

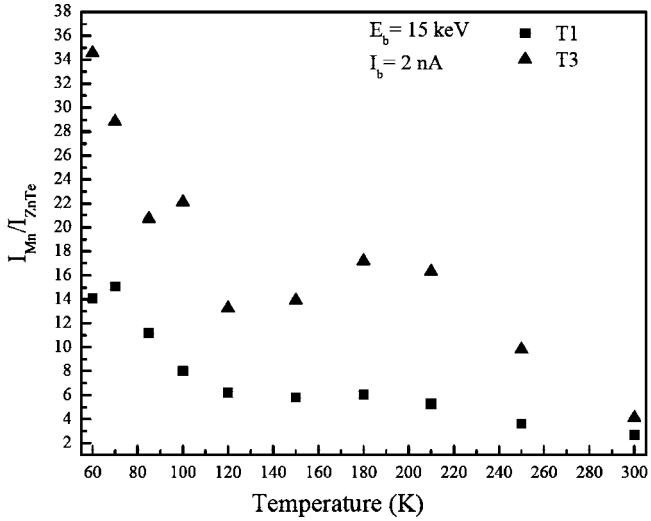

Figure 8. CL intensity ratio I_{Mn}/I_{ZnTe} as a function of temperature for samples T1 and T3.

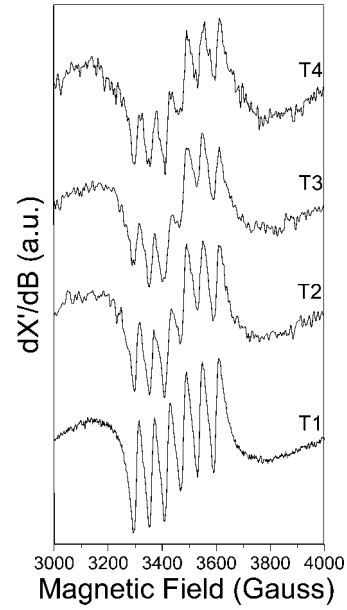

Figure 9. Room-temperature EPR spectra of the synthesized products.

exhibited the strongest Mn^{2+}-related emission at 60 K and is denoted by 100%, whereas samples T1, T2, and T4 exhibited Mn^{2+}-related emissions with comparative intensities of 16, 51, and 82%, as shown in Figure 7.

Evidence for the presence of an incomplete surface passivation of the nanosheets was acquired by examining the dependence of the Mn^{2+}-related emissions on the time of exposure to the *e*-beam, which had a beam current of 2 nA and beam energy of 15 keV. The CL intensity of the Mn^{2+}-related emission for all samples was found to decrease by 10−20% for an exposure to the e-beam for about 20 s, after which the CL intensity was found to saturate at a roughly fixed intensity, independent of the time of the remaining exposure. Such a decrease in CL intensity can be explained by an incomplete surface passivation and surface recombination effects that are caused by an accumulation and growth of carbon deposits originating from the e-beam injection at the surface. Since the nanosheets range in thickness from 20−40 nm and the electron beam penetration depth at 15 keV is ∼1.6 μm for ZnTe,[22] most of the electrons in the e-beam will emerge from the opposite side of a nanosheet, thereby causing possible carbon accumulation on the back side of the sheet as well.

The intensity of the Mn^{2+} related emission is roughly proportional to its concentration in the ZnTe nanosheets, as evidenced from the CL intensities in Figure 7. The CL intensity ratios of the Mn and ZnTe related emissions, I_{Mn}/I_{ZnTe}, are shown for samples T1 and T3 as a function of temperature in Figure 8. The defect related emissions for samples T2 and T4 prevented an analysis of this intensity ratio and is therefore not shown in Figure 8 for samples T2 and T4. The intensity ratio I_{Mn}/I_{ZnTe} decreases with increasing temperature, suggesting that capture of excited electrons (or possibly diffusing excitons) by the Mn^{2+} ion is reduced when the thermal energy exceeds activation barriers for trapping by the ion. PL measurements for $Zn_{1-x}Mn_xTe$ ($x = 0.045$) have provided evidence that bound excitons on the Mn^{2+} ion are primarily responsible for the intense emission at $T = 10$ K.[20c]

For Mn^{2+} in II−VI crystals, the intra-Mn^{2+} emission occurs as a result of the transition of electrons in the $^6A_1$ symmetric ground-state to the $^4T_1$ first excited state, associated with the crystal-field-split $3d^5$ manifold of Mn^{2+} in the II−VI crystalline environment.[21a] A transition to the $^4T_1$ excited state occurs as a result of Auger recombination of diffusing excess electrons in the crystal that are captured in the vicinity of the Mn^{2+} ion. The peak recombination wavelength of 630 nm (∼1.97 eV) is likely due to a Stoke's shift of the $^6A_1$ to $^4T_1$ excitation, which is ∼2.2 eV.[23] Furthermore, in the absence of carrier capture at the Mn^{2+} ion for high temperatures, both nonradiative and radiative recombination channels associated with defects (and possibly surface recombination) will occur, resulting in the dominant defect related emissions ($\lambda \gtrsim 650$ nm) that is particularly prominent in the CL spectra of Figure 7 for samples T2 and T4.

EPR experiments were performed at room temperature to ascertain the embedding of Mn^{2+} inside the host lattice. In the Mn-doped products, the hyperfine interaction with the ^{55}Mn nuclear spin ($I = 5/2$) gives rise to the six line spectra,[1a,24] which is also observed in our case (Figure 9). On the contrary, the resonance of Mn^{3+} cannot be observed because of the higher value of the zero-field splitting.

The hyperfine coupling constants are 55.4×10^{-4}, 55.1×10^{-4}, 55.3×10^{-4}, and 57.5×10^{-4} cm^{-1} for T1, T2, T3, and T4, respectively. These values are lower than those observed for Mn-doped ZnSe samples.[3]

According to earlier reports, with the increase in Mn concentration, hyperfine splitting is enhanced, implying reduced covalency and less coupling between the ground-

(23) Moriwaki, M. M.; Becker, W. M.; Gebhardt, W.; Galazka, R. R. *Phys. Rev. B* **1982**, *26*, 3165–3171.

(24) Koh, A. K.; Miller, D. J. *Solid State Commun.* **1986**, *60*, 217–222.

state of Mn and sp-states of the nanocrystals.[25] In our case, the hyperfine splitting values do not vary significantly with the increase in Mn concentration. Hence, it can be inferred that at higher Mn concentrations Mn^{2+} still occupies the Zn^{2+} sites in the $Zn_{1-x}Mn_xTe$ lattice. In previous reports on the EPR investigation of $Zn_{1-x}Mn_xTe$ samples, the hyperfine interaction of the Mn^{2+} nucleus collapsed at room temperature.[26] However, for T2, T3, and T4, the symmetry of the six-line spectra is hindered by a sharp absorption line centered at $g = 2.0$. The sharp line has already been observed for carbon composite and results from a graphitic layer.[1d] The broad line is attributed to dipolar interactions such as the Mn (sp band) exchange and the Mn−Mn exchange.[27] Mn also has a tendency to form pairs and clusters with an increase in the number of Mn atoms.[27] The observed sextuplet EPR signals in the nanosheets with a higher Mn concentration might arise from a non uniform distribution of Mn^{2+} between the bulk and the surface of the nanocrystals. In fact, the formation of nanorods with the catalytic effect of Mn clearly indicates that a small fraction of Mn is not incorporated in the lattice of the $Zn_{1-x}Mn_xTe$ nanosheets. Statistical analysis of the TEM images shows that the volume fraction of the nanorods is ∼0.2 and 0.4% as compared to the nanosheets in T3 and T4, respectively. Hence, the majority of the Mn^{2+} is actually inside the ZnTe lattice, corroborated by a distinct hyperfine spectrum in all the products.

In depth analysis of the magnetic properties is the central point of a DMS study. As pointed before,[28] the magnetic behavior is highly dependent on the synthetic conditions. The magnetic measurements were performed at low and high field as a function of manganese concentration on samples T1, T2 and T3. The susceptibility was investigated using a zero-field-cooled/field-cooled (ZFC/FC) routine at a field of $\mu_0 H = 0.05$ T. Figure 10 shows the results for different Mn concentrations. The susceptibility was plotted as both, a function of temperature and, in the inset, as a function of inverse temperature. All samples display a paramagnetic behavior between 120 and 300 K. On this temperature range, the inverse of the susceptibility follows a Curie law with a Curie−Weiss temperature of respectively $\theta_1 = -632 \pm 5$ K, $\theta_2 = -648 \pm 5$ K, $\theta_3 = -735 \pm 4$ K. This behavior is a clear evidence for strong antiferromagnetic coupling between the manganese atoms. The sample T3 even displays a transition from paramagnetism to antiferromagnetism below $T_{\text{Néel}} = 109 \pm 1$ K. The value appears considerably lower than the Néel temperature for pure manganese telluride ($T_{\text{Néel}} = 173$ K). A detailed analysis of the ZFC/FC shows a discrepancy between the heavily doped (T2 and T3) and the slightly doped sample (T1). For the latest, the susceptibility

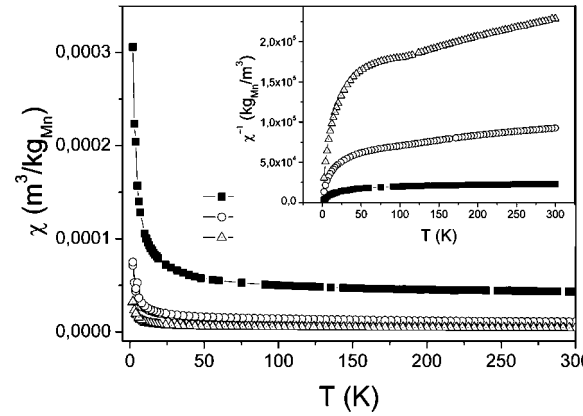

Figure 10. ZFC/FC curve measured in a field of $\mu_0 H = 0.05$ T for samples T1 (plain square), T2 (open circle), T3 (open triangle). Inset: Inverse of the susceptibility from 2 to 300 K.

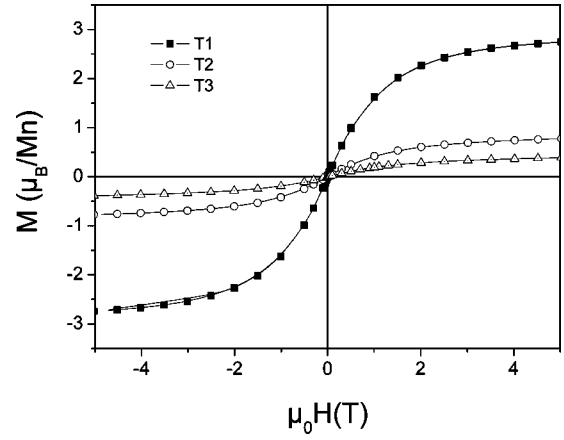

Figure 11. Hysteresis loops at $T = 2$ K for samples T1, T2, and T3.

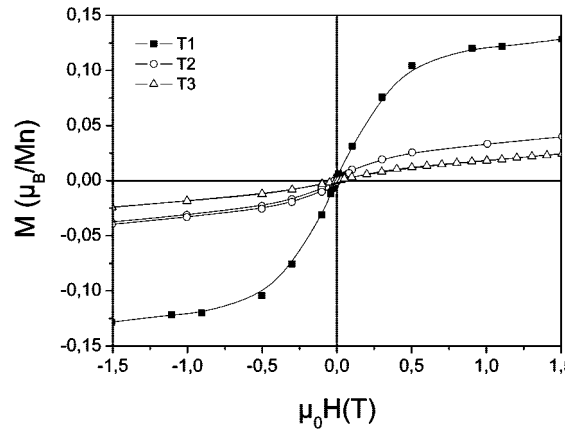

Figure 12. Hysteresis loops at $T = 300$ K for samples T1, T2, and T3.

appears to reflect the contribution of a paramagnetic phase (with antiferromagnetic interactions) and a ferromagnetic phase.

Additional high-field measurements $M(H)$ were performed at low temperature ($T = 2$ K) and room temperature ($T = 300$ K). The results are plotted in Figures 11 and 12, respectively. All the doped samples display a hysteresis at low temperature. The coercive fields are very low with a value in the range of $\mu_0 H \approx 1.0$ mT for T1, T2, and T3, respectively. The observed hysteresis could result from ferro or antiferromagnetic coupling between the manganese atoms

(25) (a) Kennedy, T. A.; Glaser, E. R.; Klein, P. B.; Bhargava, R. N. *Phys. Rev. B* **1995**, *52*, R14356–R14359. (b) Magana, D.; Perera, S. C.; Harter, A. G.; Dalal, N. S.; Strouse, G. F. *J. Am. Chem. Soc.* **2006**, *128*, 2931–2939.
(26) (a) Šoškić, Z.; Stojić, B. B; Stojić, M. *J. Phys.: Condens. Mater* **1994**, *6*, 1261–1268. (b) Brahmam, K. V.; Reddy, D. R.; Reddy, B. K. *Spectrochim. Acta, A* **2004**, *60*, 741–745.
(27) Malik, M. A.; O'Brien, P.; Revaprasadu, N. *J. Mater. Chem.* **2001**, *11*, 2382–2386.
(28) Clavel, G.; Willinger, M. G.; Zitoun, D.; Pinna, N. *Adv. Funct. Mater.* **2007**, *17*, 3159–3169.

in the ZnTe matrix. The magnetic moment does not reach saturation even at an applied field of 5 T. The magnetic moments follow a Langevin function $M(H,T) = M_T L(\mu H/k_B T)$. The hysteresis loops are plotted in Bohr magnetons per manganese atoms. The expected value for a free manganese atom in the valence +II state is 5.92 μ_B adding the spin and orbital contribution. For T1, the Langevin fit gives a value of 3.0 μ_B, a low value explained by the antiferromagnetic interactions between the Mn spins.[29] In the case of T2 and T3, the asymptotic values range below 1.0 μ_B.

All magnetic measurements (EPR and SQUID) are consistent with a +II state of the manganese atoms. The M/T magnetic measurements evidence the antiferromagnetic coupling between the spins. At room temperature, the hysteresis loops do not show a significant coercive field. Nevertheless, the behavior is still not purely paramagnetic. T1 sample (doped with 1.0% Mn) exhibits a relatively large magnetic moment of 0.12 μ_B at $\mu_0 H = 1.0$ T. This remarkable result reminds the occurrence of ferromagnetism in similar thin films.[2a] The effect is found to be tremendously enhanced compared to the thin films as the Curie temperature would be higher than 300 K.[30] In T1, the manganese atoms present two local environment with strong parallel or antiparallel coupling of the spins. The ratio between magnetization at low and room temperature gives a rough estimate of their relative abundance.

3. Conclusions

In summary, we have successfully demonstrated the direct synthesis of DMS $Zn_{1-x}Mn_xTe$ nanosheets by the efficient one-step template-free and solvent-free RAPET approach. The (111) facets form the main surfaces of the nanostructures. The Mn^{2+} is successfully doped inside the ZnTe lattice, as evidenced from EPR studies and the intense CL emission associated with the Mn^{2+} ion. The effects of temperature on the CL emission from the near-band edge, the Mn^{2+}-related emission, and defect-related emissions at longer wavelengths were examined in detail. The CL results underscore the importance of surface passivation and elimination of defects insofar as optimizing radiative recombination and emission associated with the Mn^{2+} ion. Because thin-film fabrication techniques are needed for applications in various magneto-optical, opto-electronic and spintronic devices, we believe that these nanosheets will be useful as building blocks for preparing nanometer films by self-assembly. The magnetic measurements are consistent with a Mn^{2+} state and reflect the presence of a paramagnetic phase (with antiferromagnetic coupling between the manganese atoms) and of a ferromagnetic phase.

4. Experimental Section

Zinc acetate dihydrate [$C_4H_6O_4Zn.2H_2O$, Acros Organics, 98%], manganese (II) acetate tetrahydrate [$C_4H_6O_4Mn\cdot 4H_2O$, Fluka, >99%] and tellurium powder [30 mesh, Aldrich, 99.997%], were used as received. In a typical synthesis of Mn-doped ZnTe nanostructures, 1 g of $C_4H_6O_4Zn.2H_2O$, 0.6 g of Te, and a stoichiometric amount of $C_4H_6O_4Mn\cdot 4H_2O$ (according to the Mn:Zn atomic ratio of 0, 0.01, 0.05, 0.1, and 0.2) were mixed and introduced into a 2 mL stainless steel Swagelok reactor at room temperature. The filled Swagelok reactor was tightly closed with the other plug and placed at the center of tube's furnace. The temperature of the furnace was raised to 900 °C at a rate of 10 °C/min and the temperature was maintained at 900 °C for 5 h. The Swagelok reactor was gradually cooled for 5 h to room temperature and opened inside the N_2-filled glovebox. The dry grayish products were sonicated in ethanol inside a bath sonicator for 1 h, and the dark liquid at the top was decanted to remove the contaminant carbonaceous species from the nanocrystals. The process was repeated thrice and the products were finally dried under vacuum. The yield of the $Zn_{1-x}Mn_xTe$ products were ~75%, based on the amount of the initial reactants and the carbon in the final products.

The obtained products were structurally characterized using a high-resolution scanning electron microscope (HRSEM, JSM, 7000F), a low-/high-resolution transmission electron microscope (HRTEM, JEOL, 2010), powder X-ray diffraction (Cu Kα = 1.5418 Å radiation, Bruker AXS D8), inductively coupled plasma atomic emission spectroscopy (ICP-AES; Spectroflame Module E), and energy-dispersive X-ray spectroscopy (EDS, JSM, 7000F coupled to HRSEM). An Olympus BX41 (Jobin-Yvon-Horiba) Raman spectrometer was employed, using the 514.5 nm line of an Ar ion laser as the excitation source to analyze the nature of the $Zn_{1-x}Mn_xTe$ nanosheets. The electron paramagnetic resonance (EPR) spectrum was recorded on a Bruker EPR spectrometer (ER083 CS) operating at an X-band (ν = 9.77 GHz) with a 100 kHz magnetic field modulation. The cathodoluminescence (CL) experiments were performed with a modified JEOL-5910 scanning electron microscope (SEM) using a 15 keV electron beam with a probe current of 2 nA. A GaAs:Cs (PMT) operating in the 380 to 890 nm spectral range enabled photon counting of the luminescence that was dispersed by a 0.25-m monochromator. Measurements were performed at different temperatures in the 60 to 300 K temperature range.[31] Magnetic properties were measured using a Super Quantum Interference Design (SQUID) magnetometer MPMS XL7, in the temperature range of 2−350 K and applied fields of 0−5 T. The temperature-dependent susceptibility was measured using a DC procedure. The sample was cooled to 2 K under a zero magnetic field. A low magnetic field (5 mT) was applied and data were collected from 2 to 350 K (zero-field cooled, ZFC). Field-cooled (FC) measurements were performed from 2 to 350 K with an applied field during the cooling.

Supporting Information Available: TEM images (PDF). This material is available free of charge via the Internet at http://pubs.acs.org.

CM8027737

(29) Clavel, G.; Willinger, M. G.; Zitoun, D.; Pinna, N. *Eur. J. Inorg. Chem.* **2008**, *6*, 863–868.
(30) The density and mobility of carriers and high temperature magnetic measurements on dense pellets willbe the subject of a further report.
(31) Lin, H. T.; Rich, D. H.; Konkar, A.; Chen, P.; Madhukar, A. *J. Appl. Phys.* **1997**, *81*, 3186–3195.